

SHEAR WAVE VELOCITIES IN THE UPPER CRUST OF THE QUADRILÁTERO FERRÍFERO, MINAS GERAIS: RAYLEIGH WAVE TOMOGRAPHY

Taghi Shirzad ^{1*}, Marcelo Assumpção ¹, Bruno Collaço ², Jackson Calhau ¹,
Marcelo B. Bianchi ¹, José Roberto Barbosa ¹, Raphael F. Prieto ³, Dionisio U. Carlos ³

¹Universidade de São Paulo - USP, Institute of Astronomy, Geophysics and Atmospheric Sciences - IAG, São Paulo, SP, Brazil

²Universidade de São Paulo - USP, Institute of Energy and Environment - IEE, São Paulo, SP, Brazil

³VALE S.A., São Paulo, SP, Brazil

*Corresponding author email: t.shirzad@iag.usp.br

ABSTRACT. A combination of ambient seismic noise and classical earthquake-receiver techniques was applied to characterize the shallow crustal shear-wave velocities in the Quadrilátero Ferrífero (QF), Minas Gerais state, SE Brazil, to a depth of about 4 km. Ambient seismic noise was recorded by up to 26 stations. To improve the signal of the extracted empirical Green's function (EGF), we correlated short time windows of 10 min with 70% overlapping before stacking. To test the accuracy of the retrieved EGF signals, we compared the results obtained from ambient seismic noise correlation with results from an earthquake occurred near FABR station. After measuring dispersion using frequency-time analysis (FTAN), we applied strict quality criteria (e.g., eliminating paths with residuals larger than two standard deviations, or lengths smaller than 3 wavelengths). The Fast Marching Surface wave Tomography (FMST) method was used to obtain group velocity maps. Then, the local dispersion curves were inverted to obtain a 3D Vs model. The resulting 3D model shows low velocity anomalies in the middle of the QF, compared with high velocities in the Archean part of the São Francisco Craton to the west. The low velocity metasedimentary layer in QF is about 1.5 km thick.

Keywords: seismology; inversion; tomography; surface wave; ambient seismic noise; Quadrilátero Ferrífero.

INTRODUCTION

The southern part of Minas Gerais, including the Quadrilátero Ferrífero (QF) region, is a region with relatively moderate level of seismic activity (see [Assumpção et al., 2016](#); [Bianchi et al., 2018](#)). Although previous velocity models (e.g., [Feng et al., 2007](#); [Goutorbe et al. 2015](#); [Dias et al., 2020](#)) obtained fairly good resolution on a regional scale, they do not have any resolution power needed to provide new insights into the uppermost crustal structure (upper and middle crust). However, a better knowledge of the crustal velocities is important for seismotectonic studies (micro-earthquake location improvement) as well as for

seismic hazard calculations (better estimate of site amplification), especially in the QF mining area. Short-period surface wave tomography, which did not include the QF area in previous studies (e.g., [Marchioretto and Assumpção, 1997](#); [Assumpção et al., 1997](#)), can improve velocity structural models in Minas Gerais.

Ambient seismic noise studies are an interesting alternative to the classical method of surface wave dispersion using earthquakes to create a subsurface structure model. The ambient seismic noise field is composed mostly of surface waves with random amplitude and phase which are sensitive to the crustal shear wave structure ([Wapenaar, 2004](#)). These waves

propagate in all directions, independent of a specific source, so they can be used to retrieve inter-station empirical Green's function (EGF). Ocean generated waves are the main component of the ambient seismic noise at periods 5–20 s (Webb, 1998). However, the shorter periods of ambient seismic noise are dominated by higher modes of surface waves and body waves which are mixed with fundamental modes (Bonnefoy-Claudet et al., 2006). Numerous ambient seismic noise studies have assumed uniform distribution of noise sources or energies in different azimuths as a main condition in determining accurate EGF between the stations (e.g., Snieder, 2004; Wapenaar, 2004). Recent studies regarding noise source distribution (e.g., ambient seismic noise directionality by Stutzmann et al., 2009; RMS stacking by Shirzad and Shomali, 2013; RMS-S stacking by Safarkhani and Shirzad, 2019 and 2021; RMS-SS by Xie et al., 2020) overcome the problem via separating stationary sources. We applied the WRMS (weighted root-mean-square; Shirzad et al., 2020 and 2022) stacking for these signals. The WRMS method suppresses any deviations caused by non-uniformity of sources, energy flow, and incoherent signals. Simultaneously, it enhances the EGF signal by normalizing the number of sources, source energies, and finding the coherent signals. The Quadrilátero Ferrífero is located in the southern edge of São Francisco Craton (Figure 1). This area, characterized by a Neoproterozoic greenstone belt, is overlain by a Paleoproterozoic sedimentary succession, and surrounded by older gneiss complexes.

In this paper, we use data from stations of the newest VALE seismic network (Figure 1) and Brazilian Seismographic Network (RSBR) for a Rayleigh wave tomography combining dispersion curves from ambient noise as well as from regional earthquakes or near the Quadrilátero Ferrífero region. Then, we present a shallow shear wave velocity model obtained from these waveforms. Next, the local dispersion curves, obtained from tomography, are inverted to obtain 1D and 3D shear wave models up to 4 km depth. Our results indicate the QF is generally characterized by a low velocity anomaly, while the Archean part of the São Francisco Craton appears as a relatively high velocity anomaly.

Dataset and study area

Continuous ambient seismic noise was recorded with several seismic networks deployed in the Quadrilátero Ferrífero and neighboring areas. The VALE network

(VL in Figure 1) consists of six broadband stations (Figure 1) and these seismic stations operated from July 2017 to October 2020, being the main continuous dataset in this research. The other seismic networks (including temporary and permanent stations; Figure 1a) recorded earthquakes since 1993 (Assumpção et al., 2002). All temporary and permanent seismic stations (see Table 1), which were used in this study, are broadband (120s with 100 sps), except ARCA which is a short-period station (2s with 50 sps). To increase the ray path coverage, we used 23 earthquakes (green stars in Figure 1a). Table 2 indicates the date, epicenter location, and magnitude of these earthquakes. We also selected one earthquake in 2019 which is very near to FABR station (green star surrounded by a circle in Figure 1) to check extracted EGF signals (Figure 2a) and dispersion measurements. Figure 2b shows the waveforms of this earthquake (mr 3.5; occurred on November 25th, 2019; No. 21 in Table 2) recorded by both VL (inverted black triangles in Figure 1) and RSBR (black triangles in Figure 1) networks. Ambient seismic noise waveforms of most stations at distances up to 300 km (signal-to-noise ratio; SNR > 5) were also used for further processing. All available ray path coverage is depicted in Figure 3a.

The São Francisco Craton units are covered by the Proterozoic, and the southern limit is erosional (Alkmim and Martins-Neto, 2012). The Minas-Itacolomi sequence is on top of an Archean greenstone belt, the Minas Supergroup together with the Itacolomi Group (see Figure 1b). The Quadrilátero Ferrífero, which is located between the São Francisco Craton and Minas-Itacolomi sequence, is in the foreland domain of the Mineiro belt and a partial area of the Paleoproterozoic Minas-Itacolomi sequence. A granite-greenstone belt association surrounded by granite-gneiss complexes comprise the Archean terranes of the Quadrilátero Ferrífero (Noce et al., 1998). Rio das Velhas Supergroup consists of a volcano-sedimentary sequence hosting the main gold deposits of the Quadrilátero Ferrífero (Dorr et al., 1957).

The greenstone belt is formed by the tonalitic-granodioritic intrusions. In the margins of the greenstone belt, these syn-volcanic intrusions appear partially or totally in the granite-gneiss complexes surrounding the greenstone belt. Belo Horizonte (to the north of the Quadrilátero Ferrífero), Caeté (to the northeast), Bação (in the center), and Bonfim (to the west) are complex units of the granite-gneiss terranes (Herz, 1970). The Archean units are tectonically

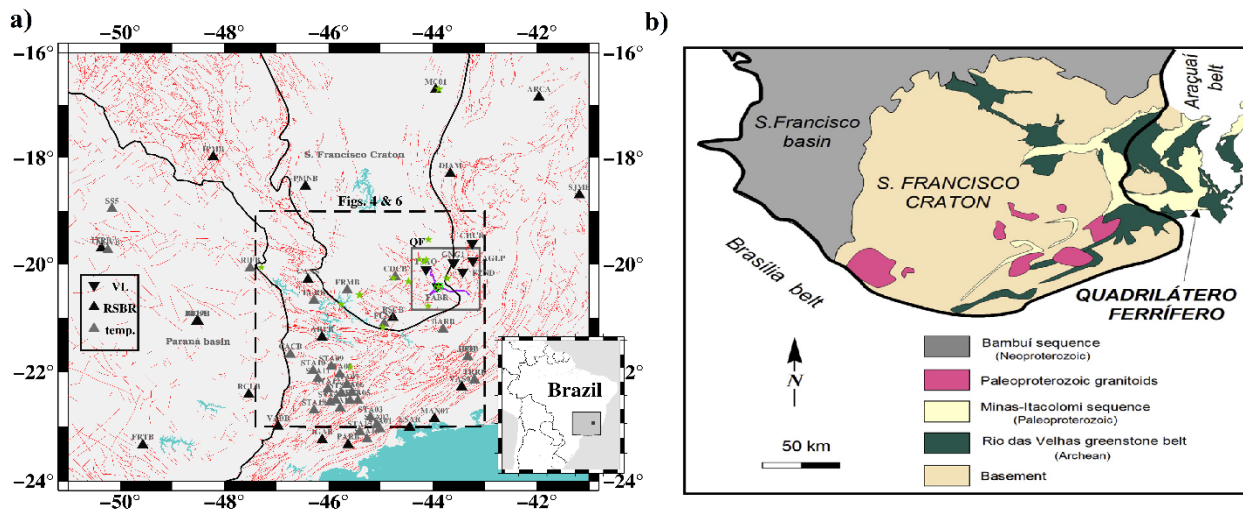


Figure 1: **a)** Study area. The light and dark grey box in the inset map shows the study area and the Quadrilátero Ferrífero region, respectively. Seismic stations are indicated by triangles (black = permanent stations since 2010; grey = older temporary stations); red lines are faults from the CPRM (Brazilian Geological Survey) database. Green stars are earthquake epicenters. Black lines are boundaries of the São Francisco Craton and Paraná basin. **b)** Simplified geological map of the southern São Francisco Craton and Quadrilátero Ferrífero mine (Alkmim and Martins-Neto, 2012).

overlain by the Proterozoic Minas Supergroup, hence comprising the Caraça (predominantly quartzites and phyllites), Itabira (mainly Lake Superior-type banded iron formation, and dolomitic carbonates with stromatolites), and Piracicaba groups (Dorr, 1969). Moreover, the main feature of the Piracicaba Group is the interbedded quartzite and phyllite containing carbonic lenses. Also, the subsurface Piracicaba Group units (Sabará Formation) are composed by phyllites, chlorite schists, conglomerates, quartzites, greywackes, and rare iron formation (Machado et al., 1992).

METHODOLOGY

Pre-processing

The concept of using the Earth's ambient seismic noise to study its structure depends on the reliability of the extracted EGFs. Some researchers (Seats et al., 2012; Shirzad and Shomali, 2013) indicated that the final EGF signal can be optimally retrieved by dividing ambient seismic noise records into shorter windows with an amount of overlapping on time windows in pre-processing step. Thus, we first divided the continuous raw data into 10-min time windows to enhance the SNR of the final inter-station EGF signal. According to the study of Pedersen et al. (2007), however, a 5-point zero-phase bandpass Butterworth pre-filtering was applied in the period range of 0.5 to 5.0 s. The standard ambient

seismic noise low frequency approach of Bensen et al. (2007) was used in this study. Therefore, after removing mean and trend, the time (one-bit) and frequency (whitening) domain normalizations were performed for all windowed signals. This step suppresses the influence of instrument irregularities, human activities, and earthquake signals.

The prepared signals are finally cross-correlated for all available station pairs, with 70% overlapping of time window. For each station pair, the 10-min cross-correlation functions (CCFs) are stacked using the WRMS stacking method as introduced by Shirzad and Assumpção (2019). The WRMS method selects and stacks all cross-correlation functions in three individual steps for each station-pair. First, the method measures the energy level within the expected signal window and selects the CCFs which sources are within the stationary zone. The expected signal window was defined based on the time window corresponding to ~2.0 to 4.2 km/s. Second, it normalizes the selected CCFs based on number of sources and energies. Finally, all coherent selected CCFs normalized are stacked to retrieve reliable inter-station EGF signal (Shirzad et al., 2020). Thus, the non-consecutive noise time windows with a weighting energy flux throughout the study area lead to retrieved stable and reliable EGF signal (Shirzad et al., 2022). Figure 2a shows extracted EGFs as a function of inter-station distance.

Table 1: Stations IDs, location (latitude, longitude).

No.	Station ID	Lon (°)	Lat (°)
1	AGLP*	-43.2278	-19.9381
2	CHCR*	-43.2403	-19.6133
3	FABR*	-43.9133	-20.4192
4	FJAO*	-44.1283	-20.1001
5	FZND*	-43.423	-20.1445
6	GNG1*	-43.6103	-19.9675
7	GNG2*	-43.6031	-19.9748
8	GNG3*	-43.5946	-19.9725
9	GNG4*	-43.6034	-19.9724
10	GNG6*	-43.5929	-19.9698
11	ARCA	-41.9597	-16.8467
12	CACB	-46.7326	-21.6802
13	FRMB	-45.6389	-20.4876
14	FURB	-46.2779	-20.6782
15	RIFB	-47.5019	-20.0737
16	CDCB	-44.7182	-20.2365
17	AGVB	-50.2331	-19.7393
18	PARB	-45.6217	-23.3382
19	AREB	-46.1234	-21.3625
20	TRRB	-43.1955	-22.1541
21	BSCB	-44.7635	-20.9986
22	BARB	-43.8	-21.22
23	BRBS	-45.5854	-22.5353
24	JFO	-43.325	-21.7272
25	JFOB	-43.3258	-21.7278
26	IGAB	-46.12	-23.25
27	ALF01	-40.7252	-20.6169
28	AQDB	-55.7	-20.48
29	BB19B	-48.5276	-21.0659
30	BDFB	-48.0148	-15.6418
31	BEB11	-48.5015	-21.0687
32	BSFB	-40.8465	-18.8313
33	CAM01	-41.6574	-21.8257
34	CANS	-46.3921	-20.2896
35	CMC01	-39.5191	-15.3601
36	DIAM	-43.66	-18.3
37	DUB01	-42.3742	-22.081
38	ESAR	-44.4403	-23.0207
39	FRTB	-49.564	-23.3439
40	FUN1	-44.9313	-21.1118
41	GDU01	-39.5753	-13.72
42	IPMB	-48.2117	-17.983
43	ITRB	-50.359	-19.7042
44	JANB	-44.3112	-15.0581
45	MAN01	-43.9641	-22.8652
46	MC01	-43.9417	-16.7074
47	NAN01	-40.1257	-17.8442
48	PCMB	-51.2619	-21.6074
49	PET01	-47.2753	-24.2901
50	PEXB	-48.3	-12.11
51	PMNB	-46.44	-18.54
52	RCLB	-47.531	-22.4191
53	RIB01	-40.3944	-19.3142
54	SJMB	-41.1847	-18.7029
55	SS5	-50.1547	-18.965
56	STA01	-45.0168	-23.0494
57	STA20	-45.9695	-22.5662
58	TIJ01	-49.0242	-25.9088
59	VABB	-46.9657	-23.0021
60	VAS01	-43.4426	-22.2801
61	TRCB	-52.634	-22.7953

Asterisk star symbols (*) indicate the stations of the VL network.

Dispersion curves

In addition to the geometrical spreading, the surface wave is dispersed in a layered medium as a function of period. The shorter periods are more sensitive to the subsurface layers, while the longer ones sample the deeper layers. Therefore, calculating these dispersion

curves can provide the earth's interior information in the different pathways. The Rayleigh wave group velocity dispersion curves were calculated using Frequency-Time Analysis (FTAN) with the multiple filter ([Dziewonski et al., 1969](#)) and the phase-matched filter ([Herrin and Goforth, 1977](#)) techniques.

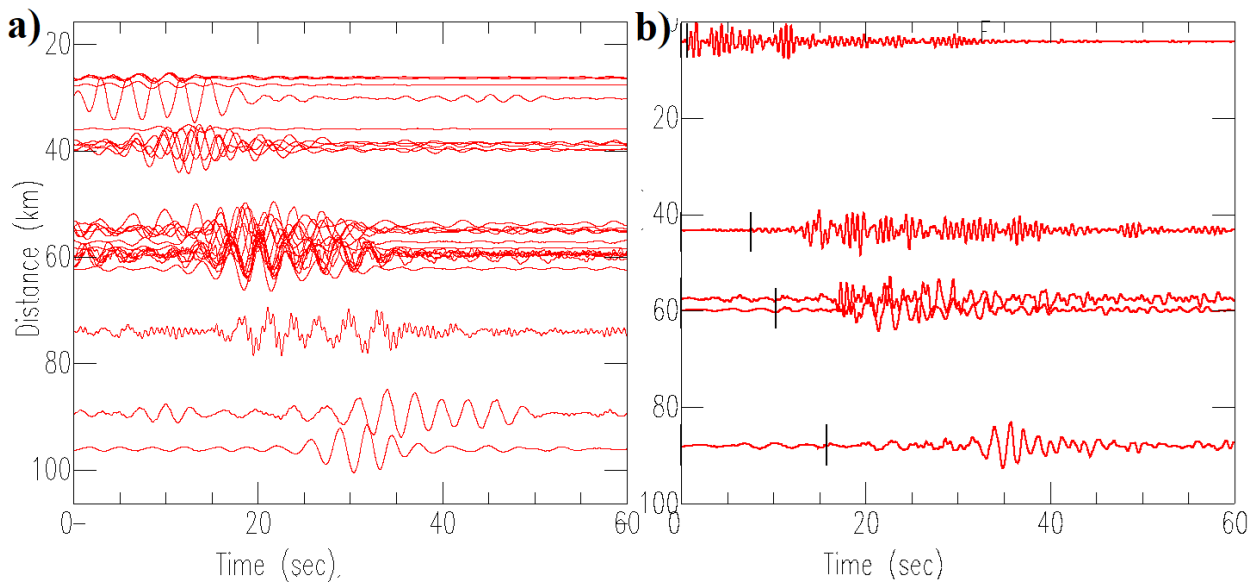


Figure 2: **a)** Inter-station EGF waveforms according to the inter-station distance filtered between 0.5 and 5.0 s. **b)** Earthquake No. 21, magnitude M_R 3.5, at different stations. Vertical marks show P-wave first arrival.

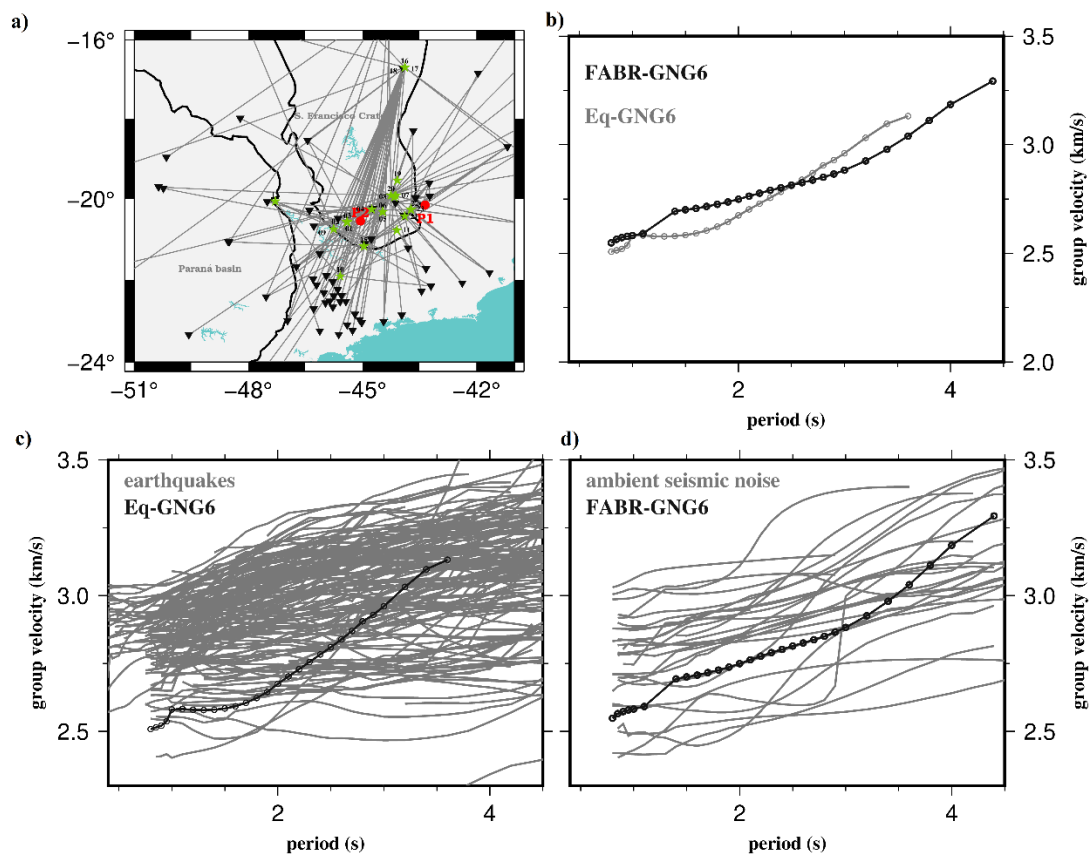


Figure 3: **a)** All ray paths (grey lines) used for tomography; both earthquake data and ambient noise. Green stars are epicenters numbered as in [Table 1](#). **b)** Rayleigh wave group velocity curves, corresponding to the 2019 earthquake registered at GNG6 station (grey line) and to the inter-station FABR-GNG6 EGF (black line). It should be noted that the Eq-GNG6 (grey line) is obtained from earthquake waveform, and FABR-GNG6 from the extracted EGF by ambient seismic noise data. **c)** all dispersion curves of waveforms of earthquakes in [Table 2](#). **d)** all dispersion curves of extracted EGFs by ambient seismic noise. In (c) and (d), the two solid-dotted lines are the dispersion measurements shown in [Figure 3b](#).

Table 2: Date, epicenter location (latitude, longitude) and magnitudes of the 23 earthquakes.

No.	Date	Lat (°)	Lon (°)	Mag
1	1993-03-09	-20.570	-45.401	3.1
2	1993-05-12	-20.576	-45.410	2.9
3	1993-09-29	-20.578	-45.395	2.4
4	1993-12-04	-20.2616	-44.751	2.6
5	1993-12-27	-20.323	-44.460	3.6
6	1993-12-28	-20.322	-44.469	3.2
7	1994-04-11	-19.917	-44.121	2.6
8	1994-04-13	-19.958	-44.162	2.3
9	1997-11-17	-20.750	-45.755	3.5
10	1998-04-16	-21.910	-45.580	2.3
11	1998-05-23	-20.780	-44.090	2.1
12	1999-04-11	-20.060	-47.290	2.9
13	2007-05-24	-15.000	-44.300	3.8
14	2007-12-09	-15.032	-44.295	4.9
15	2011-08-14	-21.176	-44.959	3.2
16	2012-05-19	-16.695	-43.883	4.0
17	2012-12-19	-16.697	-43.879	3.5
18	2012-12-19	-16.700	-43.882	3.5
19	2016-04-11	-19.540	-44.080	3.3
20	2016-05-02	-19.910	-44.250	3.5
21	2019-11-25	-20.427	-43.887	3.5
22	2020-08-07	-20.270	-43.720	2.7
23	2020-08-08	-20.260	-43.723	2.7

Applying such filters causes resolution uncertainties in the time-frequency domains (Heisenberg's uncertainty), so that larger values of the Gaussian filter width, α , increase the resolution in the frequency domain while the resolution decreases in the time domain (Mallat, 2004). Hence, a suitable Gaussian filter width, α , was set based on the distances (Shapiro and Singh, 1999). Because the epicentral distance of the 2019 earthquake to FABR-station is less than 3 km, this station is used as a reference to make comparisons with the results from the noise correlations. We used the codes of

Herrmann and Ammon (2002) for both earthquake waveforms and inter-station EGF signals to calculate Rayleigh wave group velocity dispersion curves within the expected wave signal window (~ 2.0 to 4.2 km/s) and desired period range of 0.5 sec to 4.4 sec. Also, α -values of 3 and 6 were appropriate for inter-event distances shorter and larger than 50 km, respectively, as outlined by Shapiro and Singh (1999). Figure 3b compares the dispersion curves of the 2019 earthquake registered at the GNG6 station (grey line) and of the inter-station FABR-GNG6 EGF (black line).

2D Group velocity inversion

For a given period, the synthetic data (synthetic traveltimes) can be inverted using different geographic cell sizes. Comparing the traveltimes residuals, checkerboard resolution tests, and the uncertainty results, we can determine which cell size gives optimized results (Rawlinson and Sambridge, 2003). For each period, we parameterized the study area into 35×43 grid points spaced $0.4^\circ \times 0.4^\circ$. By inverting the data (dispersion curves) and running the checkerboard resolution tests using different cell size, this model with minimum traveltimes residuals and optimum checkerboard test results was selected. The Fast Marching Surface wave Tomography, FMST (Rawlinson and Sambridge, 2005), computer code was applied to obtain 2D group velocity tomographic maps. The optimum regularization parameters (e.g., damping and smoothing) were set by standard L-curve (see Appendix A). Because the number of iterations for the subspace inversion depends on the period of the tomography (Shirzad and Shomali, 2013), we selected 2 iterations for the shorter ($T \leq 2.2$ s) and 5 for the longer ($T \geq 2.4$ s) periods. These inversion parameters as a function of period are shown in Table 3. Figures 4a-4c show the 2D group velocity maps at the periods of 0.7, 1.5 and 2.6 sec. According to the stratigraphic column of the Quadrilátero Ferrífero region by Alkmim and Marshak (1998), the shorter period ($T = 0.7$ s) was selected in the unconformity subsurface formation (with soft sediment and weathering layer), while the second period ($T = 1.5$ s) is within the mid layer of Paleoproterozoic Minas Supergroup rocks. These rocks are developed from 1100 to 2100 m as reported by Spier et al. (2006). However, the longer period ($T = 2.6$ s) was selected within the Archean granite–gneiss basement. As shown in the top maps of Figure 4, the QF is characterized by low group velocities, and the Archean part of the São Francisco Craton by high group velocities.

Depth inversion

The local dispersion curve was calculated for each geographic grid point from all computed group velocity maps at different periods. Figure 5a shows the local dispersion curves at grid points P1 (43.4°W, 20.2°S in the QF) and P2 (45.0°W, 20.5°S, in the high velocity area of the São Francisco Craton). Each local dispersion curve was inverted to obtain 1D V_s -depth profiles. For this inversion, an iterative damped least-squares inversion was applied using *surf96* code (Herrmann

and Ammon, 2002). We parameterized a half-space (from surface to 8 km depth) with multiple layers as the initial V_s model. This 1D model was divided into layers with a constant thickness (500 m) without any low velocity channel. Figure 5b shows 1D inversion models for points P1 in the QF (red) and P2 in the São Francisco Craton (blue). The calculated dispersion curves from 1D V_s at grid points P1 (V_{s-P1}) and P2 (V_{s-P2}) are shown by solid lines in Figure 5a.

Solution quality

Checkerboard test

Before further processing and interpretation, the synthetic checkerboard test can give us an evaluation of the lateral resolution (Lévéque et al., 1993). First, we generated a synthetic model with small perturbations disposed of in a grid pattern with alternative anomalies, $U_0 \pm 0.5$ km/s (Schultz and Crosson, 1996). Then, the synthetic forward traveltimes were calculated using this perturbed model for each ray path that we used in the inversion procedure of the observed data at a given period. Finally, the synthetic traveltimes were inverted. The inversion procedure was done by the original parameters including cell size, and regularization parameters (damping and smoothing) which had been used in the inversion of observed data. Figures 4d-4f show the recovered checkerboard resolution test at the periods of 0.7, 1.5 and 2.6 sec. The checkerboard test was repeated with different block sizes as described in Appendix B for which the result maps are shown in Figure B.

Sensitivity kernel

Some researchers (e.g., Yang et al., 2007; Huang et al., 2010) used one-third of the wavelength as the effective depth range of surface wave dispersion. However, we used a single scattering Born approximation assuming constant velocity layers (Zhou et al., 2004) to obtain the depth sensitivity kernel function of the Rayleigh wave group velocity. Figure 5c indicates the normalized sensitivity kernel function at periods of 0.7, 1.0, 2.0, 3.0, 4.0, 4.4 s. As shown in this figure, the minimum (0.7 s) and maximum (4.4 s) depth functions of the group velocity are in the range of ~0.3 and ~5 km.

Uncertainties of Initial V_s

To consider the effect of the initial V_s value on obtained V_s model, we used the stochastic measurement. Therefore, we perturbed the Initial V_s model 300 times by a normal random distribution with a standard deviation of 0.3 km/s (Naghavi et al., 2019).

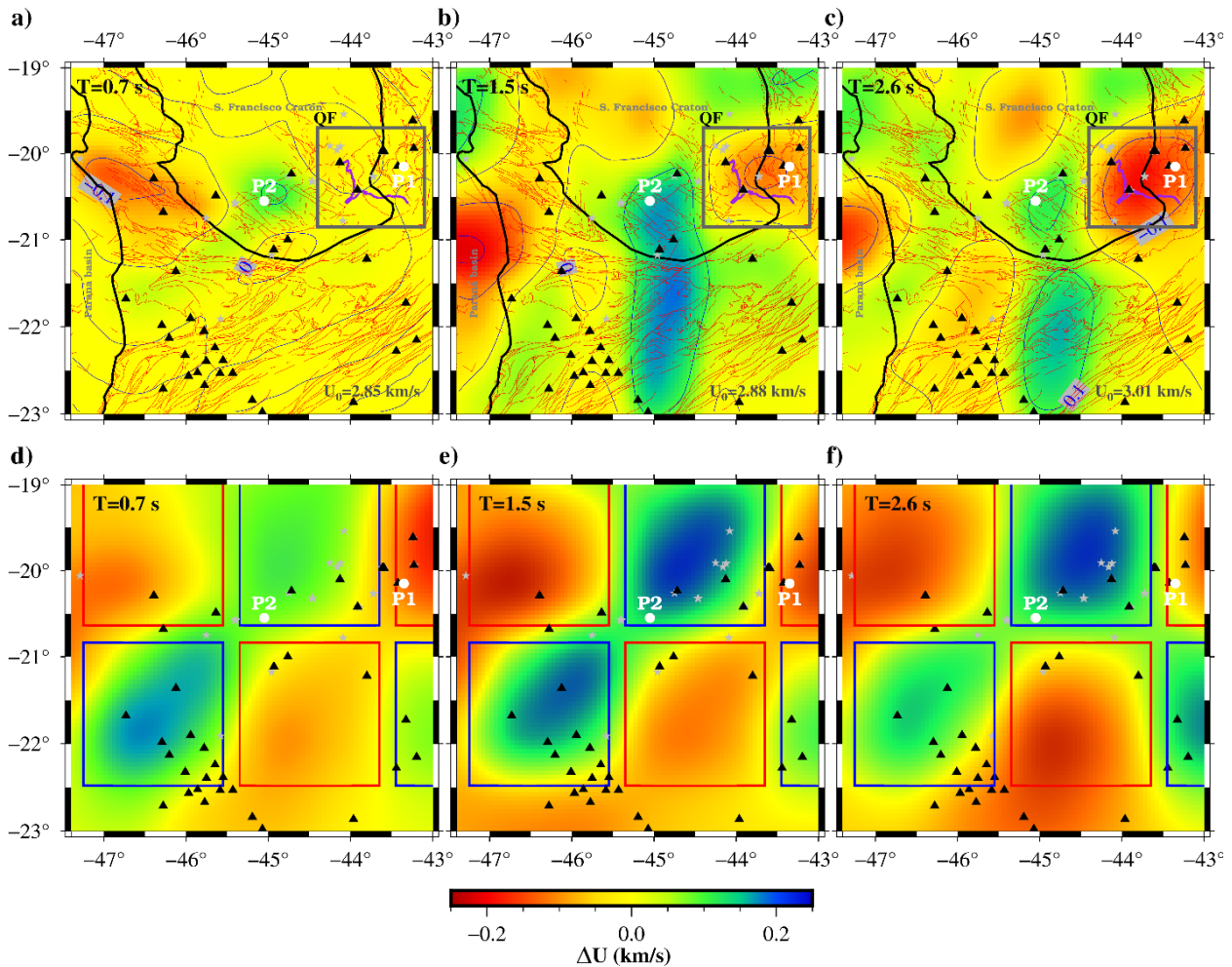


Figure 4: Top maps show the Rayleigh wave group velocity results at the periods of 0.7, 1.5 and 2.6 sec. Background reference velocities are at the right bottom of each map. The thin black lines are velocity contours every 0.1 km/s; the thick purple lines correspond to the Moeda and Engenho Faults; the thick black lines are the limits of the São Francisco Craton and the Paraná basin. Bottom maps represent the checkerboard resolution test results for three periods. The input anomalies are shown by red and blue boxes with $U_0 \pm 0.5$ km/s. Two white circles indicate the two grid points, **P1** (43.4°W, 20.2°S) and **P2** (45.0°W, 20.5°S).

The local dispersion curves at grid points P1 and P2 with original regularization were inverted with these perturbed initial models. The light grey models in [Figure 5b](#) show the calculated V_s 1D models. The average of these light grey models is depicted by a black 1D V_s model for P1 and P2 separately.

DISCUSSION

In ambient seismic noise studies, the period range and the spatial coverage are controlled by the inter-station distances ([Bensen et al., 2007](#)), their azimuthal orientations ([Shirzad et al., 2022](#)), and the number of coincident recorded days ([Shirzad and Shomali, 2014](#)). The period range of extracted EGF controls the maximum depth range and depth resolution of the shear wave models. A reasonable similarity was

observed between the dispersion curves of the earthquake and inter-station EGF (e.g., Eq-GNG6 and FABR-GNG6; [Figure 3b](#)). Thus, we can infer that reliable inter-station EGF signals were extracted in the interesting period range. Moreover, any bias between the dispersion curves can be originated from the directionality of the energy flow, extreme Earth scatterers, etc. (see [Shirzad et al., 2022](#)).

Depth inversion of surface waves can adequately resolve the velocity anomalies, although the depth ([Calkins et al., 2011](#)) and the topography of the different horizons ([Guo et al., 2013](#)) are less well constrained, due to the 1D regularization parameters (smoothness). The 1D V_s models generally picture out two main layers (e.g., see 1D model of **P1** and **P2** in [Figure 5b](#)). The upper layer thickness varies between

Table 3: Period, number of earthquake (Eq.) and ambient noise (AN) rays (NR), background group velocity (U_0), and damping value as a function of the period.

T (sec)	NR		U_0 (km/s)	damp
	Eq.	AN		
0.7	69	11	2.852	14.5
0.8	65	19	2.831	16.0
0.9	66	26	2.816	19.5
1.0	70	27	2.822	20.5
1.1	73	27	2.837	20.5
1.2	77	26	2.848	21.0
1.3	79	26	2.858	23.0
1.4	83	26	2.867	23.5
1.5	84	27	2.882	24.0
1.6	87	27	2.894	26.0
1.7	90	27	2.904	25.5
1.8	90	27	2.914	25.5
1.9	93	27	2.922	26.0
2.0	93	27	2.931	26.5
2.2	92	25	2.945	25.5
2.4	92	25	2.969	25.5
2.6	91	25	2.986	25.0
2.8	91	25	3.004	24.5
3.0	89	24	3.015	24.0
3.2	85	24	3.030	22.0
3.4	83	23	3.034	21.0
3.6	79	20	3.035	20.5
3.8	77	17	3.055	20.0
4.0	76	16	3.071	19.5
4.2	75	11	3.087	18.0
4.4	68	10	3.086	15.0

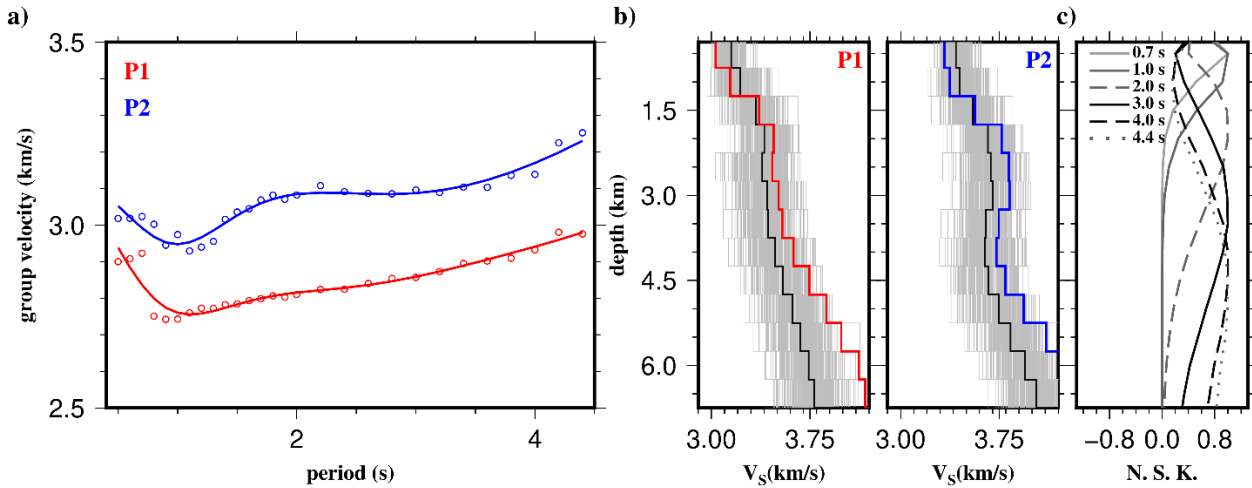


Figure 5: **a)** Local dispersion curves depicted by open circles, corresponding to two grid points, **P1** (red) situated at 43.4°W, 20.2°S, in QF, and **P2** (blue) situated at 45.0°W, 20.5°S, in SFC. **(b)** 1D velocity models for the grid points **P1** (red) and **P2** (blue). The calculated dispersion curves from V_{s-P1} and V_{s-P2} models are shown by solid lines in **(a)**. The light grey models in **(b)** show the stochastic estimate of the model uncertainty due to different initial models. The average of these light grey models is depicted by the solid black line. The colored (red and blue) lines are the best fitting model. **(c)** shows normalized sensitivity kernel (N. S. K.) as a function of depth at period of 0.7 (minimum; light grey solid line), 1.0 (dark grey solid line), 2.0 (dashed light grey line), 3.0 (black solid line), 4.0 (dashed black line), and 4.4 (maximum; dotted line) s. According to the sensitivity kernel function at the minimum and maximum periods, the minimum and maximum depths are 0.3 and ~5 km, respectively.

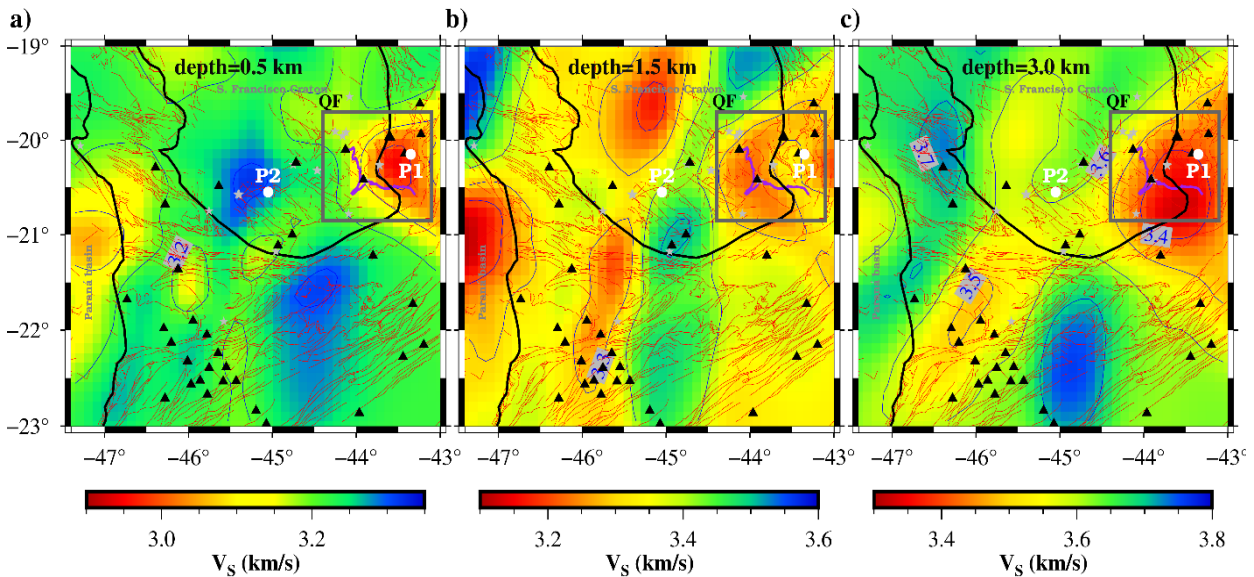


Figure 6: Horizontal slice of shear wave velocity, V_s , at the depths of 0.5, 1.5 and 3.0 km. The thick purple lines indicate the Moeda and Engenho Faults delimiting the low velocities of the QF. The thick black lines indicate the limits of the São Francisco Craton and the Paraná basin. Station and events are shown by triangles and stars. **P1** and **P2** are shown by white circles.

1-2 km. After calculating all 1D models, the 2D V_s model can be prepared as horizontal maps (Figure 6). At a shallower depth (0.5 km; Figure 6a), a low velocity anomaly is observed to the north and east of the Engenho and Moeda faults (inside the grey box), where metamorphic rocks predominate. Higher velocities are found in the shield, Archean area of the São Francisco

Craton, composed mainly of granitic and gneissic rocks which is consistent with expected rock velocities (e.g., Christensen and Mooney, 1995) and similar to the ones found by Marchioreto and Assumpção (1997). Moreover, relatively low velocity is present in Paraná Basin, and some parts of Brasília belt. In addition to the QF low velocity anomaly, at intermediate depth (1.5

km in [Figure 6b](#)), the São Francisco Basin (Bambuí sedimentary layer) appears as a low velocity region (see [Figure 1b](#)), while the São Francisco Craton and Araçuaí belt have high velocities, especially where Paleoproterozoic granitoids predominate (see [Figure 1b](#)). At greater depth (3 km in [Figure 6c](#)), the QF still has low velocities compared to the neighboring areas.

The center part of the QF, composed mainly of metasedimentary rocks of the Caraça and Nova Lima groups ([Alkmim and Martins-Neto, 2012](#)), presents low velocities at all depths. The metasedimentary layer of the QF is about 1 to 2 km thick ([Figure 6](#)). The QF basement also presents lower V_S (~3.6 km/s) compared to the SFC area to the west (~3.75 km/s). These values are consistent with the preliminary results of [Marchioreto and Assumpção \(1997\)](#).

CONCLUSION

A combination of the inter-station EGF and (micro-) earthquake waveforms can be used to obtain the subsurface velocity structure, especially at depths up to 5 km. This study presents a shear wave velocity model of the shallow layers of the Quadrilátero Ferrífero. Similar characteristics, presented in earthquake dispersion and inter-station EGF, indicate that our dispersion curves are reasonably accurate. The 1D V_S models present a bottom layer overlaid by an upper layer with a varied thickness between 1-2 km. The 2D V_S maps show lower velocities in the QF center region, characterized by ~1.5 km thick layer of metasedimentary rocks. To the west of the QF, the São Francisco Craton presents higher velocities, typical of exposed granitic and gneissic rocks. In addition, the obtained velocity model can be used to improve locations of the local (micro-) earthquakes where previous poor upper crustal model could have large location and source parameter uncertainties.

ACKNOWLEDGEMENT

This study used data provided by the VALE QF network and the Brazilian Seismographic Network (RSBR). The VL data are not openly available, but they can be shared upon request to VALE and IAG-USP. The first author, T.S., thanks the Fundação de Amparo à Pesquisa do Estado de São Paulo (FAPESP), São Paulo, Brazil (project 2013/24215-6 and grant 2016/20952-4). The authors thank Wanderson Tenório (VALE) for field maintenance of the QF seismic network. The known faults are from the CPRM database (<http://www.cprm.gov.br>). Some figures were

made using Generic Map Tools, GMT, version 6.2.0 ([Wessel et al., 2013](#)). Also, the authors would like to thank the Editor and two anonymous reviewers for their constructive comments and useful suggestions.

APPENDICES

Appendix A

The general relationship between data (d) and model parameters (m), $d=g(m)$, is the basis of the tomographic method ([Menke, 1989](#)). The difference $d^{obs}-g(m_0)$ can provide an indication of how well the current model predictions satisfy the data, where m_0 is an initial model. The inverse problem is done to minimize the difference between observed and predicted data using an appropriate regularization. The regularization parameters are important in all inversion steps because geophysical tomographic problems are often under-determined or mixed-determined in nature ([Menke, 1989](#)). A regularization term is usually added to the objective function to reduce the non-uniqueness of the solution. Thus, the optimum regularization parameters should be found by an acceptable trade-off between satisfying the data and finding a model with the minimum amount of structural variation. Large regularization values lead to a predicted model similar to the initial model while the data misfit is large. In contrast, little regularization causes a better fit between d^{obs} and d^{cal} , but the model variance can be large. The optimum regularization parameters are obtained by visual inspection of the data misfit and model roughness trade-off curve, described by the L-curve. Thus, by several single-iteration inversions with a range of regularization values ([Eberhart-Phillips, 1986; 1993](#)), we can obtain the optimum parameters. [Figures A1](#) and [A2](#) show the L-curve for obtaining the optimum damping and smoothing values at the period of 1.5 s, respectively. For this period, we run the tomography procedure for a range of damping values (grey circles). The optimum damping minimizes the data and model variances simultaneously, indicated by the red circle.

Appendix B

We carried out different inversions using various block sizes in order to investigate the stability of the inversion results. For a given period, 1.5 s, we inverted the synthetic data (dispersion curves used in [Figure 4e](#)) when the size is the half ([Figure B1](#)), triple ([Figure B2](#)) and quadruple ([Figure B3](#)) of the size of its original value ([Figure 4](#)).

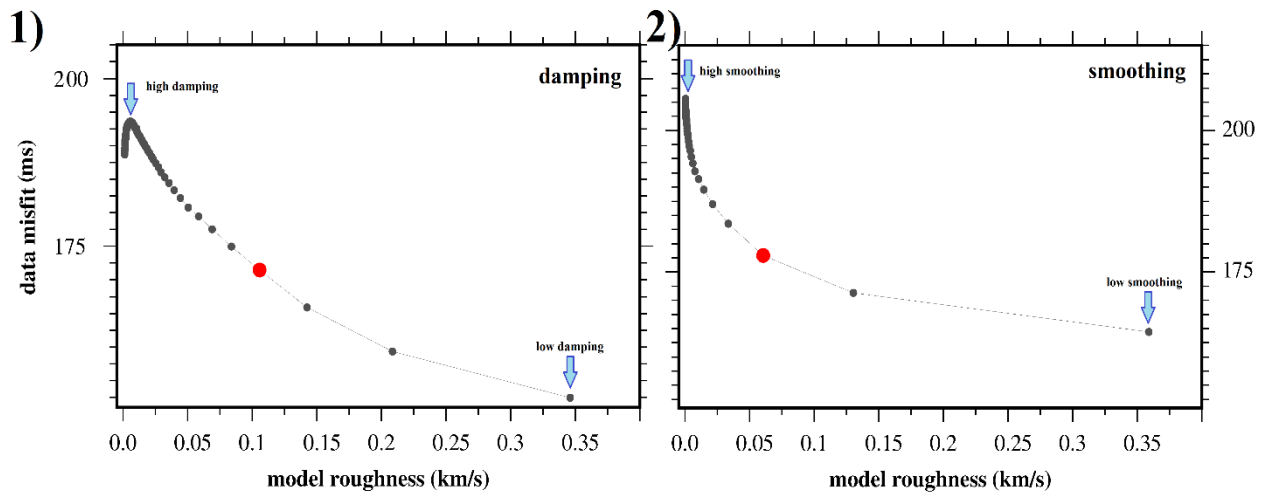


Figure A: Schematic illustration of a trade-off curve used to find optimum (red circle) damping (1) and smoothing (2) parameters for an inversion at the period of 1.5 sec.

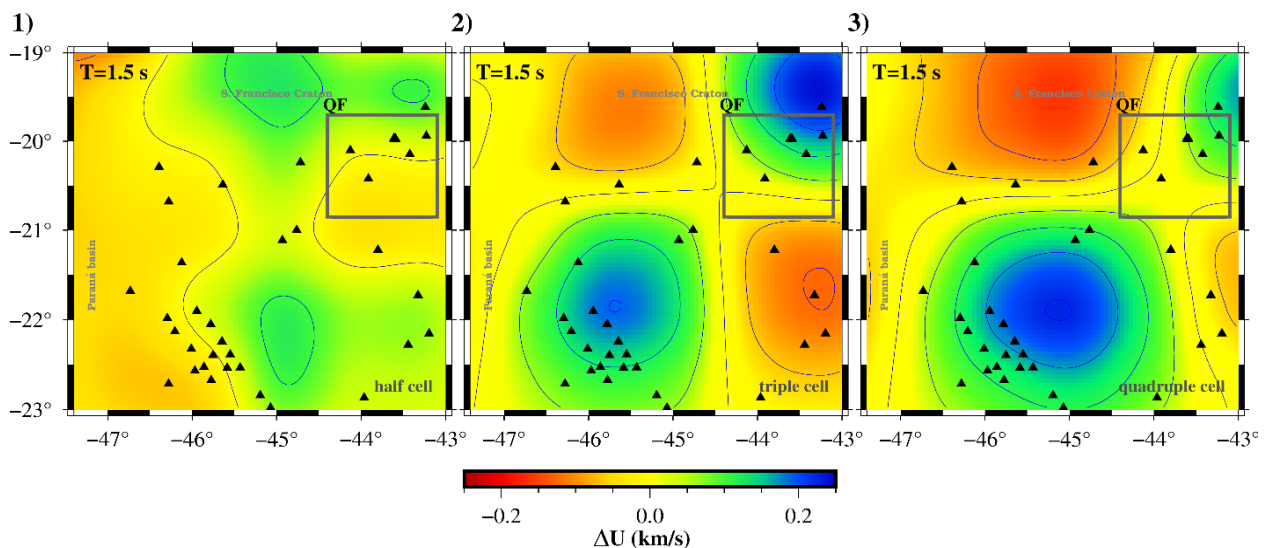


Figure B: For period 1.5 s, the inverted synthetic data (dispersion curves used in Figure 4e) retrieve the checkerboard models when the block size is a (1) half, (2) triple and (3) quadruple of the cell size used in the original test (Figure 4).

REFERENCES

- Alkmim, F.F., and S. Marshak, 1998, Transamazonian orogeny in the São Francisco craton, Minas Gerais, Brazil: evidence for Paleoproterozoic collision and collapse in the Quadrilátero Ferrífero: *Precambrian Research*, **90**, 29–58. DOI: [10.1016/S0301-9268\(98\)00032-1](https://doi.org/10.1016/S0301-9268(98)00032-1).
- Alkmim, F.F., and M.A. Martins-Neto, 2012, Proterozoic first-order sedimentary sequences of the São Francisco craton, eastern Brazil: *Marine and Petroleum Geology*, **33**, 127–139. DOI: [10.1016/j.marpetgeo.2011.08.011](https://doi.org/10.1016/j.marpetgeo.2011.08.011).
- Assumpção, M., J.R. Barbosa, J. Berrocal, A.M. Bassini, J.A.V. Veloso, V.I. Mârza, M.G. Huelsen, and L.C. Ribotta, 1997, Seismicity patterns and focal mechanisms in southeastern Brazil: *Rev. Bras. Geof.*, **15**, 2, 119–132. DOI: [10.1590/S0102-261X1997000200002](https://doi.org/10.1590/S0102-261X1997000200002).
- Assumpção, M., D. James, and A. Snoke, 2002, Crustal thicknesses in SE Brazilian shield by receiver function analysis: implications for isostatic compensation: *J. Geophys. Res.*, **107**, B1, ESE2-1—ESE2-14. DOI: [10.1029/2001JB000422](https://doi.org/10.1029/2001JB000422).
- Assumpção, M., S.L. Dias, I. Zevallos, and J.B. Naliboff, 2016, Intraplate stress field in South America from earthquake focal mechanisms: *Journal of South American Earth Sciences*, **71**, 278–

295. DOI: [10.1016/j.jsames.2016.07.005](https://doi.org/10.1016/j.jsames.2016.07.005).
- Bensen, G.D., M.H. Ritzwoller, M.P. Barmin, A.L. Levshin, F. Lin, M.P. Moschetti, N.M. Shapiro, and Y. Yang, 2007, Processing seismic ambient noise data to obtain reliable broad-band surface wave dispersion measurements: *Geophys. J. Int.*, **169**, 1239–1260. DOI: [10.1111/j.1365-246X.2007.03374.x](https://doi.org/10.1111/j.1365-246X.2007.03374.x).
- Bianchi, M.B., M. Assumpção, M.P. Rocha, J.M. Carvalho, P.A. Azevedo, S.L. Fontes, F.L. Dias, J.M. Ferreira, A.F. Nascimento, M.V. Ferreira, and I.S.L. Costa, 2018, The Brazilian Seismographic Network (RSBR): Improving Seismic Monitoring in Brazil: *Seismological Research Letters*, **89**, 2A, 452–457. DOI: [10.1785/0220170227](https://doi.org/10.1785/0220170227).
- Bonnefoy-Claudet, S., F. Cotton, and P.-Y. Bard, 2006, The nature of noise wavefield and its applications for site effects studies: a literature review: *Earth Sci. Rev.*, **79**, 3, 205–227. DOI: [10.1016/j.earscirev.2006.07.004](https://doi.org/10.1016/j.earscirev.2006.07.004).
- Calkins, J.A., G.A. Abers, G. Ekström, K.C. Creager, and S. Rondenay, 2011, Shallow structure of the Cascadia subduction zone beneath western Washington from spectral ambient noise correlation: *Journal of Geophysical Research*, **116**, B07302. DOI: [10.1029/2010JB007657](https://doi.org/10.1029/2010JB007657).
- Christensen, N. I., and W. D. Mooney, 1995, Seismic Velocity Structure and Composition of the Continental Crust: A Global View: *Journal of Geophysical Research: Solid Earth*, **100**, 9761–9788. DOI: [10.1029/95JB00259](https://doi.org/10.1029/95JB00259).
- Dias, F. L., M. Assumpção, P. S. Peixoto, M. B. Bianchi, B. Collaço, and J. Calhau, 2020, Using seismic noise levels to monitor social isolation: An example from Rio de Janeiro, Brazil: *Geophysical Research Letters*, **47**, e2020GL088748. DOI: [10.1029/2020GL088748](https://doi.org/10.1029/2020GL088748).
- Dorr, J.V.N., 1969, Physiographic stratigraphic and structural development of the Quadrilátero Ferrífero, Minas Gerais, Brazil: U.S. Geological Survey, Professional Paper, 641–A, A1–A110. DOI: [10.3133/pp641A](https://doi.org/10.3133/pp641A).
- Dorr, J.V.N., J.E. Gair, J.G. Pomerene, and G.A. Rynearson, 1957, Revisão da estratigrafia pré-cambriana do Quadrilátero Ferrífero: DNPM-DFPM, Rio de Janeiro, Brazil, 31 p. (Avulso 81).
- Dziewonski, A., S. Bloch, and M. Landisman, 1969, A technique for the analysis of transient seismic signals: *Bull. Seismol. Soc. Am.*, **59**, 427–444. DOI: [10.1785/BSSA0590010427](https://doi.org/10.1785/BSSA0590010427).
- Eberhart-Phillips, D., 1986, Three-dimensional velocity structure in the northern California Coast Ranges from inversion of local earthquake arrival times: *Bull. Seismol. Soc. Am.*, **76**, 1025–1052. DOI: [10.1785/BSSA0760041025](https://doi.org/10.1785/BSSA0760041025).
- Eberhart-Phillips, D., 1993, Local earthquake tomography: earthquake source regions, *in* Iyer, H.M., and K. Hirahara, Eds., *Seismic Tomography: Theory and Practice*: Chapman and Hall, London, 613–643, chapter 22.
- Feng, M., S. van der Lee, and M. Assumpção, 2007, Upper mantle structure of South America from joint inversion of waveforms and fundamental mode group velocities of Rayleigh waves: *J. Geophys. Res.*, **112**, B04312. DOI: [10.1029/2006JB004449](https://doi.org/10.1029/2006JB004449).
- Goutorbe, B., D.L.O. Coelho, and S. Drouet, 2015, Rayleigh wave group velocities at periods of 6–23 s across Brazil from ambient noise tomography: *Geophysical Journal International*, **203**, 2, 869–882. DOI: [10.1093/gji/ggv343](https://doi.org/10.1093/gji/ggv343).
- Guo, Z., X. Gao, H. Shi, and W. Wang, 2013, Crustal and uppermost mantle S-wave velocity structure beneath the Japanese islands from seismic ambient noise tomography: *Geophysical Journal International*, **193**, 394–406. DOI: [10.1093/gji/ggs121](https://doi.org/10.1093/gji/ggs121).
- Herrin, E., and T. Goforth, 1977, Phase-matched filters: Application to the study of Rayleigh Waves, *Bull. Seism. Soc. Am.*, **67**, 1259–1275. DOI: [10.1785/BSSA0670051259](https://doi.org/10.1785/BSSA0670051259).
- Herrmann, R.B., and C.J. Ammon, 2002, Computer programs in seismology-surface waves, receiver functions and crustal structure. Saint Louis University, Department of Earth and Atmospheric Sciences, Missouri, USA. Available on: <http://www.eas.slu.edu/People/RBHerrmann/ComputerPrograms.html>
- Herz, N., 1970, Gneissic and igneous rocks of the Quadrilátero Ferrífero, Minas Gerais, Brazil: U.S. Geological Survey Professional Paper, 641-B: B1–B58. DOI: [10.3133/pp641B](https://doi.org/10.3133/pp641B).
- Huang, Y.-C., H. Yao, B.-S. Huang, R.D. van der Hilst; K.-L. Wen, W.-G. Huang, C.-H. Chen, 2010, Phase velocity variation at periods 0.5–3 s in the Taipei basin of Taiwan from correlation of ambient seismic noise: *Bull. Seism. Soc. Am.*, **100**, 5A, 2250–2263. DOI: [10.1785/0120090319](https://doi.org/10.1785/0120090319).
- Lévêque, J.-J., L. Rivera, and G. Wittlinger, 1993, On the use of the checkerboard test to assess the resolution of tomographic inversion: *Geophysical Journal International*, **115**, 1, 313–318. DOI: [10.1111/j.1365-246X.1993.tb05605.x](https://doi.org/10.1111/j.1365-246X.1993.tb05605.x).
- Machado, N., C.M. Noce, E.A. Ladeira, O.A. Belo de Oliveira, 1992, U-Pb geochronology of Archean magmatism and Proterozoic metamorphism in the Quadrilátero Ferrífero, southern São Francisco Craton, Brazil: *Geological Society of America Bulletin*, **104**, 1221–1227. DOI: [10.1130/0016-7606\(1992\)104<1221:UPGOAM>2.3.CO;2](https://doi.org/10.1130/0016-7606(1992)104<1221:UPGOAM>2.3.CO;2).
- Mallat, S., 2004, *A Wavelet Tour of Signal Processing*: Academic Press, 832 pp.
- Marchioreto, A., and M. Assumpção, 1997, Inversão Tomográfica com ondas Rayleigh no sul do Cráton do São Francisco e Faixa de Dobramentos Brasília-Uruaçu: 5th International Congress of the Brazilian Geophysical Society, Nov 1997, cp-299-00320. DOI: [10.3997/2214-4609-pdb.299.322](https://doi.org/10.3997/2214-4609-pdb.299.322).

- Menke, M., 1989, *Geophysical Data Analysis: Discrete Inverse Theory*: Academic Press, 302 pp.
- Naghavi, M., M.R. Hatami, T. Shirzad, and H. Rahimi, 2019, Radial Anisotropy in the Upper Crust Beneath the Tehran Basin and Surrounding Regions: *Pure and Applied Geophysics*, **176**, 787–800. DOI: [10.1007/s00024-018-1986-7](https://doi.org/10.1007/s00024-018-1986-7).
- Noce, C.M., N. Machado, and W. Teixeira, 1998, U-Pb geochronology of gneisses and granitoids in the Quadrilátero Ferrífero (Southern São Francisco Craton): age constraints for Archean and Paleoproterozoic magmatism and metamorphism: *Revista Brasileira de Geociências*, **28**, 95–102. DOI: [10.25249/0375-7536.199895102](https://doi.org/10.25249/0375-7536.199895102).
- Pedersen, H. A., and F. Krüger, 2007, Influence of the seismic noise characteristics on noise correlations in the Baltic shield: *Geophys. J. Int.*, **168**, 197–210. DOI: [10.1111/j.1365-246X.2006.03177.x](https://doi.org/10.1111/j.1365-246X.2006.03177.x).
- Rawlinson, N., and M. Sambridge, 2005, The fast marching method: an effective tool for tomographic imaging and tracking multiple phases in complex layered media: *Exploration Geophysics*, **36**, 4, 341–350. DOI: [10.1071/EG05341](https://doi.org/10.1071/EG05341)
- Safarkhani, M., and T. Shirzad, 2019, Improving C¹ and C³ Empirical Green's Functions from ambient seismic noise in NW Iran using RMS ratio stacking method: *Journal of Seismology*, **23**, 787–799. DOI: [10.1007/s10950-019-09834-1](https://doi.org/10.1007/s10950-019-09834-1).
- Safarkhani, M., and T. Shirzad, 2021, Improvement in the Empirical Green's Function Extraction Using Root Mean Square Ratio Stacking: *Journal of the Earth and Space Physics*, **46**, 4, 39–48. DOI: [10.22059/jesphys.2020.281801.1007119](https://doi.org/10.22059/jesphys.2020.281801.1007119)
- Schultz, A.P., and R.S. Crosson, 1996, Seismic velocity structure across the central Washington Cascade Range from refraction interpretation with earthquake sources: *Journal of Geophysical Research*, **101**, B12, 27899–27915. DOI: [10.1029/96JB02289](https://doi.org/10.1029/96JB02289).
- Seats, K.J., J.F. Lawrence, and G.A. Prieto, 2012, Improved ambient noise correlation functions using Welch's method: *Geophys. J. Int.*, **188**, 513–523. DOI: [10.1111/j.1365-246X.2011.05263.x](https://doi.org/10.1111/j.1365-246X.2011.05263.x).
- Shapiro, N.M., and S.K. Singh, 1999, A systematic error in estimating surface-wave group-velocity dispersion curves and a procedure for its correction: *Brief Report, Bull. Seismol. Soc. Am.* **89**, 4, 1138–1142. DOI: [10.1785/BSSA0890041138](https://doi.org/10.1785/BSSA0890041138).
- Shirzad, T., and M. Assumpção, 2019, Extracting optimum interstation empirical Green's function in west-central Brazil: 3rd Brazilian Seismology Symposium, Vinhedo, São Paulo, Brazil.
- Shirzad, T., and Z.H. Shomali, 2013, Shallow crustal structures of the Tehran basin in Iran resolved by ambient noise tomography: *Geophys. J. Int.*, **196**, 1162–1176. DOI: [10.1093/gji/ggt449](https://doi.org/10.1093/gji/ggt449).
- Shirzad, T., and Z.H. Shomali, 2014, Shallow crustal radial anisotropy beneath the Tehran basin of Iran from seismic ambient noise tomography: *Physics of the Earth and Planetary Interiors*, **231**, 16–29. DOI: [10.1016/j.pepi.2014.04.001](https://doi.org/10.1016/j.pepi.2014.04.001).
- Shirzad, T., M. Assumpção, and M. Bianchi, 2020, Ambient seismic noise tomography in west-central and Southern Brazil, characterizing the crustal structure of the Chaco-Paraná, Pantanal and Paraná basins: *Geophysical Journal International*, **220**, 3, 2074–2085. DOI: [10.1093/gji/ggz548](https://doi.org/10.1093/gji/ggz548).
- Shirzad, T., M. Safarkhani, and M. Assumpção, 2022, Extracting reliable empirical Green's functions using weighted cross-correlation functions of ambient seismic noise in West-Central and Southern Brazil: *Geophys. J. Int.*, **230**, 2, 1441–1464. DOI: [10.1093/gji/ggac126](https://doi.org/10.1093/gji/ggac126).
- Snieder, R., 2004, Extracting the Green's function from the correlation of coda waves: a derivation based on stationary phase: *Phys. Rev. E.*, **69**, 046610. DOI: [10.1103/PhysRevE.69.046610](https://doi.org/10.1103/PhysRevE.69.046610).
- Spier, C. A., P. M. Vasconcelos, and M. B. Oliveira, 2006, ⁴⁰Ar/³⁹Ar geochronological constraints on the evolution of lateritic iron deposits in the Quadrilátero Ferrífero, Minas Gerais, Brazil, *Chemical Geology*, **234**, 1–2, 79–104. DOI: [10.1016/j.chemgeo.2006.04.006](https://doi.org/10.1016/j.chemgeo.2006.04.006).
- Stutzmann, E. M., Schimmel, G. Patau, and A. Maggi, 2009, Global climate imprint on seismic noise: *Geochem. Geophys. Geosyst.*, **10**, 11, Q11004. DOI: [10.1029/2009GC002619](https://doi.org/10.1029/2009GC002619).
- Wapenaar, K., 2004, Retrieving the elastodynamic Green's function of an arbitrary inhomogeneous medium by cross correlation: *Phys. Rev. Lett.*, **93**, 254301. DOI: [10.1103/PhysRevLett.93.254301](https://doi.org/10.1103/PhysRevLett.93.254301).
- Webb, S.C., 1998, Broadband seismology and noise under the ocean: *Rev. Geophys.*, **36**, 105–142. DOI: [10.1029/97RG02287](https://doi.org/10.1029/97RG02287).
- Wessel, P., W.H.F. Smith, R. Scharroo, J. Luis, and F. Wobbe, 2013, *Generic Mapping Tools: Improved Version Released*: Eos, Transactions, American Geophysical Union, **94**, 45, 409. DOI: [10.1002/2013EO450001](https://doi.org/10.1002/2013EO450001).
- Xie, J., Y. Yang, Y. Luo, 2020, Improving cross-correlations of ambient noise using an rms-ratio selection stacking method: *Geophys. J. Int.*, **222**, 2, 989–1002. DOI: [10.1093/gji/ggaa232](https://doi.org/10.1093/gji/ggaa232).
- Yang, Y., M.H. Ritzwoller, A.L. Levshin, and N.M. Shapiro, 2007, Ambient noise Rayleigh wave tomography across Europe: *Geophysical Journal International*, **168**, 259–274. DOI: [10.1111/j.1365-246X.2006.03203.x](https://doi.org/10.1111/j.1365-246X.2006.03203.x).
- Zhou, Y., F.A. Dahlen, and G. Nolet, 2004, Three-dimensional sensitivity kernels for surface wave observables: *Geophysical Journal International*, **158**, 142–168. DOI: [10.1111/j.1365-246X.2004.02324.x](https://doi.org/10.1111/j.1365-246X.2004.02324.x).

Shirzad, T.: conceptualization, formal analysis, software, result validation, visualization, figure plotting, manuscript writing and editing; **Assumpção, M.:** supervision, conceptualization, data preparation, methodology, manuscript writing and editing, result validation, visualization; **Collaço, B.:** field work, data preparation, discussions; **Calhau, J.:** field work, data curation, data preparation; **Bianchi, M.:** Data curation, data preparation, database management, discussions; **Barbosa, J.R.:** field work, preliminary data analyses; **Prieto, R.F.:** field work, data management, discussions; **Carlo, S.D.U.:** field work, data management, discussions.

Received on December 21, 2021 / Accepted on September 28, 2022